Three-dimensional structure determination protocol for noncrystalline biomolecules using x-ray free-electron laser diffraction imaging

Tomotaka Oroguchi and Masayoshi Nakasako*

Department of Physics, Faculty of Science and Technology, Keio University, 3-14-1 Hiyoshi, Kohoku-ku, Yokohama, Kanagawa 223-8522, Japan and Research Infrastructure Group, Advanced Photon Technology Division, RIKEN Harima Institute, 1-1-1 Kouto, Mikaduki, Sayo, Hyogo, Japan

(Received 27 August 2012; revised manuscript received 17 December 2012; published 19 February 2013)

Coherent and intense x-ray pulses generated by x-ray free-electron laser (XFEL) sources are paving the way for structural determination of noncrystalline biomolecules. However, due to the small scattering cross section of electrons for x rays, the available incident x-ray intensity of XFEL sources, which is currently in the range of 10^{12}–10^{13} photons/μm^2/pulse, is lower than that necessary to perform single-molecule diffraction experiments for noncrystalline biomolecules even with the molecular masses of megadalton and submicrometer dimensions. Here, we propose an experimental protocol and analysis method for visualizing the structure of those biomolecules by the combined application of coherent x-ray diffraction imaging and three-dimensional reconstruction methods. To compensate the small scattering cross section of biomolecules, in our protocol, a thin vitreous ice plate containing several hundred biomolecules/μm^2 is used as sample, a setup similar to that utilized by single-molecule cryoelectron microscopy. The scattering cross section of such an ice plate is far larger than that of a single particle. The images of biomolecules contained within irradiated areas are then retrieved from each diffraction pattern, and finally provide the three-dimensional electron density model. A realistic atomic simulation using large-scale computations proposed that the three-dimensional structure determination of the 50S ribosomal subunit embedded in a vitreous ice plate is possible at a resolution of 0.8 nm when an x-ray beam of 10^{16} photons/500×500 nm^2/pulse is available.

DOI: 10.1103/PhysRevE.87.022712 PACS number(s): 87.15.B−, 68.37.Yz, 87.64.Bx

I. INTRODUCTION

Since its discovery in the last century, x-ray diffraction has made great contributions to the structural determination of crystallized biomolecules at atomic resolution. However, along with the advances in structural biology, it has been revealed that most proteins function in the form of molecular assemblies, which are difficult or impossible to crystallize. (Other structural analysis methods such as NMR also have difficulties due to the limitations on molecule size.) Therefore, there is a strong need for structural analysis methodologies of biomolecules without crystallization. The recent advances in the theory of x-ray diffraction, as well as the development of new x-ray sources, have enhanced the prospect for such structural analyses.

Coherent x-ray diffraction imaging (CXDI) [1–5] is a promising technique for visualizing the three-dimensional (3D) structures of noncrystalline molecular assemblies and micron- to submicron-sized particles with nanometer-level resolution. CXDI is a lensless imaging method free from aberration. The method enables determination of the electron density of a sample particle, which is projected along the incident x-ray beam, from the oversampled Fraunhofer diffraction pattern. The weak electromagnetic interaction of x rays with electrons enables the penetration into thick samples and the Born approximation in the scattering process.

Over the last decade, researchers have explored the potential application of CXDI to the imaging of noncrystalline materials. In addition, new methods have been proposed for the structural determination of noncrystalline biomolecules, combining single-particle diffraction imaging techniques [6–8] and intense and fully coherent x-ray free-electron laser (XFEL) pulses [9,10]. Recently, a CXDI experiment at the Linac Coherent Light Source (LCLS) [9] visualized the projection images of the giant mimivirus at a resolution of 40 nm [11] using an XFEL pulse of 10^{12} photons/μm^2/pulse and a liquid jet injector [12], demonstrating the capabilities of the XFEL-CXDI method.

In this study, we propose another feasible experimental protocol for future noncrystalline biomolecule diffraction experiments. The protocol targets thin vitreous ice plates containing several hundred biomolecules/μm^2 as a sample (Fig. 1), a setup similar to that utilized by single-molecule cryoelectron microscopy (cryo-EM). The intensities and resolution in the diffraction patterns of ice containers would be improved compared to those of single biomolecules, because samples consisting of both water molecules and hundreds of target biomolecules have a far larger scattering cross section than that of a single biomolecule. In addition, the XFEL pulses would easily hit target biomolecules, which are present in arbitrary locations of the ice plate.

In our proposed protocol, using a microfocused x-ray beam with a size of 0.5–1.0 μm^2 [13], a number of single-shot diffraction patterns are recorded during the translational movement of the ice plate (Fig. 1). The projection image is retrieved from each oversampled diffraction pattern, which has emerged

*Author to whom correspondence should be addressed: nakasako@phys.keio.ac.jp

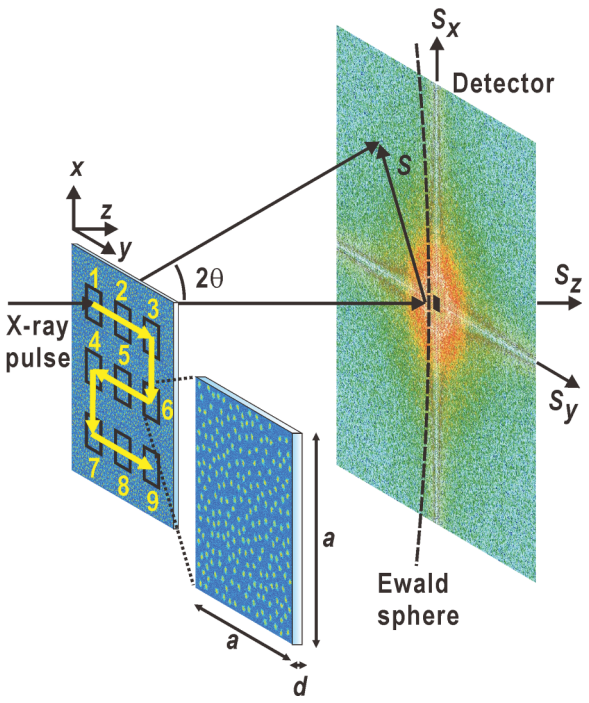

FIG. 1. (Color online) Schematic illustration of an XFEL-CXDI experiment for a thin vitreous ice plate of thickness d. During the translational motion of the ice plate as illustrated, x rays with a cross section of $a \times a$ irradiate different positions of the ice plate, and a large number of diffraction patterns are collected within a short period of time.

from the whole irradiated area of the vitreous ice plate. Therefore, each retrieved image, in principle, would contain hundreds of biomolecules, which are in various orientations relative to the incident x-ray beam. Then, as proposed in our previous study [14], a 3D electron density map of targeted particles is then modeled by applying a 3D-reconstruction method [15] that was originally developed for EM analysis.

The application of liquid jet injectors to single-molecule diffraction imaging has been studied theoretically [7,16,17]. but the structural analyses of biomolecules embedded in thin layers of vitreous ice have not yet been proposed or investigated. As the other approach, the reciprocal-space correlation method has been proposed and applied to *ab initio* reconstruction of an image of a single particle from fluctuations in the diffraction pattern from several copies, randomly oriented about an axis [18,19]. In contrast, in our protocol, the 3D reconstruction is performed for real-space projection images, which are phase retrieved from the diffraction pattern of a vitreous ice containing several hundred particles. Therefore, our protocol is quite different from the reciprocal-space correlation method.

To examine the feasibility of our protocol, we have conducted a series of simulations on diffraction imaging of ice plates explicitly composed of 229 50S ribosomal subunits and 429 590 000 water molecules. The results have demonstrated that the 3D structure of the 50S ribosomal subunit can be successfully determined from diffraction patterns of thin plates of vitreous ice containing sample molecules. We also examined the feasibility and limitations of our proposed protocol through simulations by taking various experimental parameters into consideration, such as incident intensity of the x-ray pulse and thickness of the ice plates. The 50S ribosomal subunit is a representative macromolecular complex, and the structural studies conducted in the last four decades [20,21] have provided density maps of the 50S ribosomal subunit at various resolutions. This point facilitates the evaluation of the proposed protocol.

II. COMPUTATIONAL METHODS

A. Outline of simulation

When a thin vitreous ice plate, which contains a number of biomolecules, is irradiated by a square-shaped x-ray beam of dimensions $a \times a$ with uniform intensity I_0 and wavelength λ (Fig. 1), the diffraction intensity $I(\vec{S})$ at scattering vector $\vec{S}(=2\sin\theta/\lambda)$ of the scattering angle 2θ is described by Eq. (1).

$$I(\vec{S}) = I_0\, r_e^2 \left(\frac{\lambda}{\sigma a}\right)^2 \left[\left|\sum_i^{Np}\sum_j^{Np} F_{Pi}(\vec{S})^* F_{Pj}(\vec{S})\right|^2 + |F_w(\vec{S})|^2 + \left\{\sum_i^{Np} F_{Pi}(\vec{S})\right\}\cdot F_w(\vec{S})^* + \left\{\sum_i^{Np} F_{Pi}(\vec{S})\right\}^*\cdot F_w(\vec{S})\right], \tag{1}$$

where $F_{Pi}(\vec{S})$ and $F_w(\vec{S})$ are the structure factors of the ith particle and the irradiated area of the vitreous ice plate, respectively; r_e is the classical electron radius; N_p represents the number of rigid particles. We assumed that those particles are distributed within the irradiation area with random orientation and there are no overlaps between particles along the direction of the incident x-ray beam. In Eq. (1), the first term originates only from the particles and is indispensable for the structure analysis. However, it is impossible to experimentally extract only the first term from the diffraction pattern in reciprocal space. In contrast, when we return to real space by using the phase-retrieval method, each projection image is simply composed of the electron densities of particles and the vitreous ice region, and therefore only particle images can be easily isolated (Fig. 1). The 3D-reconstruction method in real space is then applied to the projection images of particles.

In this study, we simulated a diffraction experiment and structure analysis protocol for eight 50-nm-thick vitreous ice plates, each containing 229 copies of the 50S ribosomal subunit, impinged on by an x-ray beam with a cross section of 500×500 nm^2. The magnitude of electron density fluctuation of the vitreous ice region in the projection map is of critical importance to define the border of particle images as discussed in our previous study [14]. This point was taken into account when conducting our simulations, to approach more realistic data considerations. The vitreous ice plates were composed of explicit water molecules, the positions of which were obtained from molecular dynamics (MD) simulations. When assuming the x-ray wavelength of 0.06 nm, the shortest wavelength possible from the SACLA XFEL source [10], the maximum

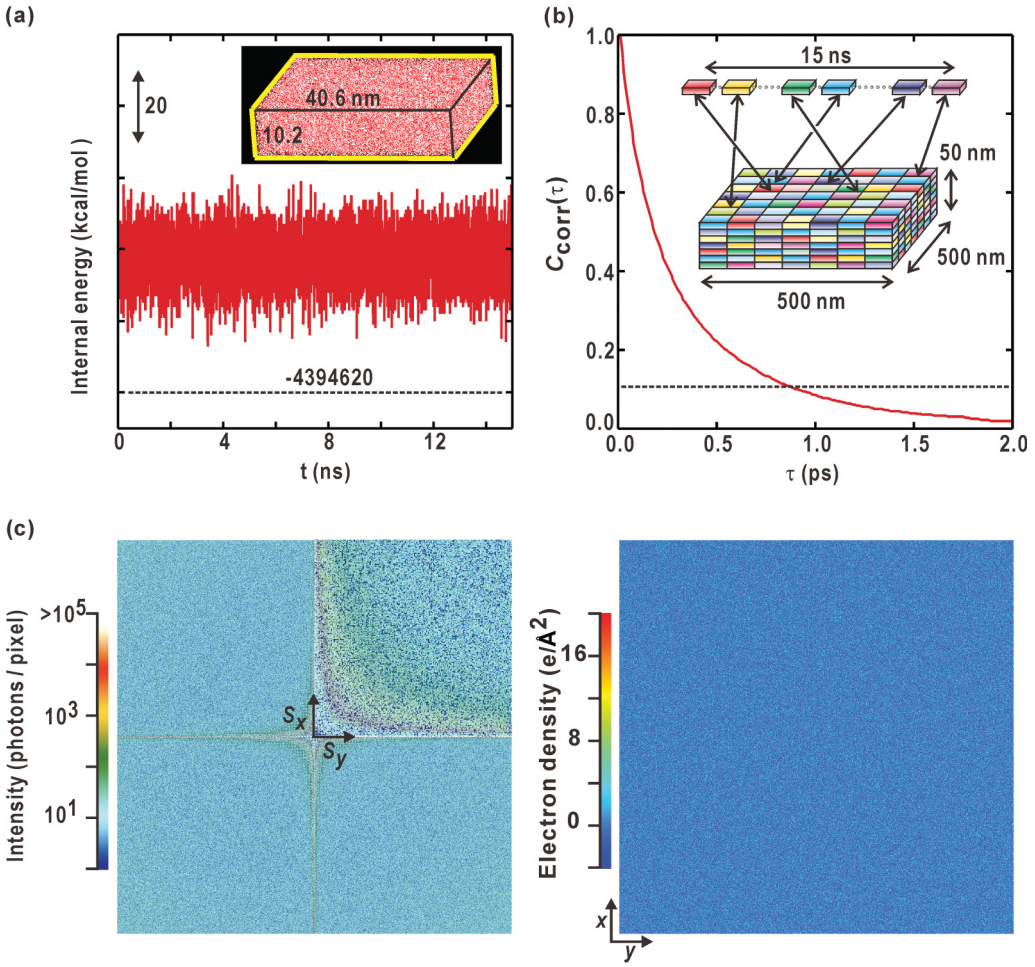

FIG. 2. (Color online) (a) Variation of the internal energy of the water block during the production MD run. The inset is a schematic illustration of the small block of water after the equilibration run. Red and white dots indicate the positions of oxygen and hydrogen atoms of water molecules, respectively. (b) Plot showing structural relaxation inside the small block of water as monitored by the time-averaged correlation function $C_{\rm corr}(\tau)$. A thin vitreous ice plate of $500 \times 500 \times 50$ nm^3 is constructed by arranging a $12.5 \times 12.5 \times 5$ array of snapshots selected from the 15-ns MD trajectory as illustrated in the inset. (c) Diffraction pattern calculated from the thin ice plate with the dimensions of $500 \times 500 \times 50$ nm^3 (left panel) and the phase-retrieved projection image of the plate (right) obtained from the diffraction pattern.

resolution of the simulation was 0.8 nm based on a geometrical consideration regarding the curvature of the Ewald sphere as described in Sec. II D.

B. Preparation of structure models of vitreous ice plate

We prepared atomic models of ice plates with dimensions of $500 \times 500 \times 50$ nm^3 by arranging the snapshots obtained from the molecular dynamics (MD) simulation of a small block of water. The block contained 549 881 TIP3P [22] water molecules, which is the maximum number manageable in the available computer system [Fig. 2(a)]. The MD simulation was conducted at 298 K using the program MARBLE [23]. The periodic boundary condition was applied with the particle-mesh Ewald method [24]. The symplectic integrator for rigid bodies [25] was used with a time step of 2 fs, during which each water molecule was treated as a rigid body.

The water block with the dimensions of $40.6 \times 40.6 \times 10.2$ nm^3 was first subjected to an energy minimization of 50 000 steps. A subsequent equilibration run of 1 ns under *NPT* conditions [23,26] of $T = 298.15$ K and $P = 1.0$ atm resulted in an equilibrated volume of $40.2 \times 40.2 \times 10.1$ nm^3 (density of 1.01 g/cm^3). Finally, a product run of 15 ns with a time step of 2 fs was performed under *NVT* conditions of $T = 298.15$ K, and snapshots were stored at every 0.5 ps. No drift in the internal energy of the system was observed, as demonstrated in Fig. 2(a).

Thin vitreous ice plates with dimensions of $500 \times 500 \times 50$ nm^3 were prepared by arranging 845 snapshots from the MD trajectory into a $12.5 \times 12.5 \times 5$ array without redundancy [Fig. 2(b)]. The snapshots were selected randomly, but any pair of snapshots in the array had little structural correlation, as described below. The period of time necessary for structural relaxation of the water block was estimated through analyzing the snapshots obtained at 10-fs resolution from the MD trajectory that was obtained under *NVT* conditions at $T = 298.15$ K. We used a correlation function to measure the structural similarity between two snapshots at times t

and $t+\tau$ as follows:

$$C(t,t+\tau)=\frac{\int_0^a\{\rho_{2D}(x,y;t)-\rho_{2D}^0\}\{\rho_{2D}(x,y;t+\tau)-\rho_{2D}^0\}dxdy}{\sqrt{\int_0^a\{\rho_{2D}(x,y;t)-\rho_{2D}^0\}^2dxdy}\sqrt{\int_0^a\{\rho_{2D}(x,y;t+\tau)-\rho_{2D}^0\}^2dxdy}},$$
$$\rho_{2D}(x,y;t)=\int_0^d\rho(x,y,z;t)\,dz, \tag{2}$$
$$\rho_{2D}^0=\frac{1}{A^2}\int_0^a\int_0^a\rho_{2D}(x,y;t)\,dxdy,$$

where $\rho(x,y,z;t)$ is the 3D electron density at time t, and $\rho_{2D}(x,y;t)$ is its projected density along the z axis. The correlation function is defined for the fluctuation of the projected density from the average ρ_{2D}^0. Parameters a and d are the dimensions of the block, and the grid size for the calculation was 0.4 nm. The structural similarity between any pair of snapshots with the time interval of τ was then calculated by time-averaging the correlation function as $C_{\rm corr}(\tau)=\langle C(t,t+\tau)\rangle$ along the 100-ps MD trajectory. The calculated $C_{\rm corr}(\tau)$ monotonously decreased and was less than 0.1 when τ was longer than 0.9 ps [Fig. 2(b)].

From the analysis, we prepared vitreous ice plates so that any pair of snapshots in the $12.5\times12.5\times5$ array has the time interval of longer than 1 ps, which was sufficient to lose structural similarity. In fact, no Bragg-like peaks, which typically arise from the arrangement of blocks with structural correlation, were observed in the diffraction patterns of any prepared ice plate, and the phase-retrieved projection density maps displayed almost uniform density of $136.0\pm1.8\,e/\text{Å}^2$ [Figs. 2(c) and 2(d)].

C. Structural model of vitreous ice containing 50S ribosomal subunit

We estimated the number of nonredundant projection images necessary for the 3D reconstruction of 50S ribosomal subunit at 0.8-nm resolution. It was approximately 1800, as calculated by dividing the solid angle of the hemisphere $(4\pi/2)$ by the fraction of the solid angle corresponding to 0.8×0.8 nm^2 on a sphere of 25-nm diameter, which roughly approximated the size of the 50S ribosomal subunit. The atomic coordinates of the 50S ribosomal subunit were downloaded from the Protein Data Bank (accession code: 1VQ8) [27]. A total of 1832 nonredundant orientations were generated in the polar-coordinate plane (θ,φ) [28] using the following equation:

$$\theta_j=\cos^{-1}\frac{2j-1-J}{J},\quad \phi_j=\sqrt{\pi J}\sin^{-1}\frac{2j-1-J}{J},$$
$$\left(j=\frac{J}{2},\frac{J+1}{2},\ldots,J\right), \tag{3}$$

where $J/2$ is the number of orientations. After 229 50S ribosomal subunits were embedded in each vitreous ice plate, water molecules that overlapped or closely contacted 50S ribosomal subunits were excluded based on biomolecular hydration [29].

D. Resolution of the simulation

Projection images are only retrieved from diffraction patterns in small-angle regions where the Ewald sphere [30] is approximated as a plane normal to the incident x-ray beam. We estimated the maximum resolution based on the geometrical consideration that a speckle size from the ice plate with the thickness of 50 nm is smaller than the separation of the Ewald sphere from the plane of $S_z=0$ along S_z (Fig. 3). Assuming that diffraction patterns are collected at an oversampling (OS) ratio [31] of 2 in one dimension, the x-ray wavelength λ and the maximum resolution in the scattering vector length $S_{\rm max}$ are related as follows:

$$\frac{1}{\lambda}-\left(\frac{1}{\lambda^2}-S_{\rm max}^2\right)^{1/2}<S_{\rm sep}. \tag{4}$$

When a CCD detector with a pixel size of 50 μm and a sample-to-detector distance of 4 m is used, $1/S_{\rm max}$ is approximately 1.2 nm ($S_{\rm sep}=\frac{1}{50}$ nm^{-1}). Based on the estimation, the diffraction pattern using x rays with the wavelength of 0.06 nm was calculated up to a resolution of 0.8 nm at the edge (Fig. 3).

E. Calculation of diffraction patterns

Diffraction patterns were calculated using Eq. (1) under the conditions shown in Table I. The structure factor of a thin ice plate at scattering vector $\vec{S}$ is expressed as the sum of

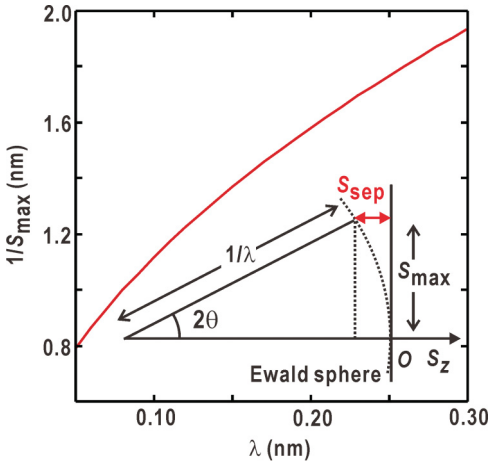

FIG. 3. (Color online) Plot showing the variation of $1/S_{\rm max}$ depending on the x-ray wavelength. The geometry in the reciprocal space for the diffraction experiment is schematically illustrated in the inset.

TABLE I. Simulation parameters for eight ice plates with a volume of $500 \times 500 \times 50$ nm^3 under the influence of Poisson noise.

Simulation	Plate No. 1	Plate No. 2	Plate No. 3	Plate No. 4	Plate No. 5	Plate No. 6	Plate No. 7	Plate No. 8
Diffraction patterns								
Size of diffraction pattern (pixels)	2560×2560	2560×2560	2560×2560	2560×2560	2560×2560	2560×2560	2560×2560	2560×2560
OS ratio (S_x and S_y directions)	4 (2,2)	4 (2,2)	4 (2,2)	4 (2,2)	4 (2,2)	4 (2,2)	4 (2,2)	4 (2,2)
S/pixel (nm^{-1})	9.95×10^{-4}	9.95×10^{-4}	9.95×10^{-4}	9.95×10^{-4}	9.95×10^{-4}	9.95×10^{-4}	9.95×10^{-4}	9.95×10^{-4}
Maximum S (nm^{-1})	1.27	1.27	1.27	1.27	1.27	1.27	1.27	1.27
X-ray wavelength (nm)	0.06	0.06	0.06	0.06	0.06	0.06	0.06	0.06
Incident x-ray intensity (photons/500×500 nm^2/pulse)	5.0×10^{16}	5.0×10^{16}	5.0×10^{16}	5.0×10^{16}	5.0×10^{16}	5.0×10^{16}	5.0×10^{16}	5.0×10^{16}
I ($S = 0$)	6.74×10^{10}	6.74×10^{10}	6.74×10^{10}	6.74×10^{10}	6.74×10^{10}	6.74×10^{10}	6.74×10^{10}	6.74×10^{10}
Phase retrieval								
Size of the support (pixels)	1280×1280	1280×1280	1280×1280	1280×1280	1280×1280	1280×1280	1280×1280	1280×1280
Pixel width (nm)	0.393	0.393	0.393	0.393	0.393	0.393	0.393	0.393
Number of support update cycles	2500	2500	2500	2500	2500	2500	2500	2500
HIO cycles per support update	4	5	20	20	4	10	20	20
Initial SW parameter α	3.0	1.5	3.0	3.0	3.0	3.0	1.5	1.5
Reduction rate of α after every support update	0.995	0.990	0.995	0.995	0.995	0.995	0.990	0.990
Final γ (%)	0.396	0.402	0.403	0.398	0.393	0.380	0.384	0.400
Correlation between the original and retrieved images	0.87	0.86	0.89	0.88	0.87	0.90	0.90	0.90
3D reconstruction								
Parameter of Gaussian low-pass filter				9–72				
Resolution of projection images in the final refinement (nm)				0.393				
Estimated resolution from the FSC value of 0.143 (nm)				0.842				

contributions from 50S ribosomal subunit and water regions:

$$F(\vec{S}) = \sum_i F_i^{50S}(\vec{S}) + F^{\text{water}}(\vec{S}),$$
$$F_i^{50S}(\vec{S}) = \sum_j f_{ij}(\vec{S}) \exp[2\pi i \vec{S} \cdot \vec{r}_{ij}], \quad (5)$$
$$F^{\text{water}}(\vec{S}) = \sum_k f_k(\vec{S}) \exp[2\pi i \vec{S} \cdot \vec{r}_k],$$

where $\vec{r}_{ij}$ represents the coordinate of the jth atom in the ith 50S ribosomal subunit, and $\vec{r}_k$ is the position of the kth water molecule. The atomic scattering factors were calculated using the following equation:

$$f(\vec{S}) = \sum_{\ell=1}^{4} a_\ell \exp\left(-\frac{b_\ell S^2}{4}\right) + c_\ell. \quad (6)$$

The coefficients a_ℓ, b_ℓ, and c_ℓ were taken from the standard table [32]. To reduce calculation costs, hydrogen atoms were not included in the calculation. Poisson noise of diffraction patterns was generated using the protocol described in the literature [33].

F. Phase-retrieval calculation for diffraction patterns

The phase-retrieval calculation was conducted by the combinational use of the hybrid-input-output (HIO) [34] and shrink-wrap (SW) [35] algorithms. The size of the support was initially set to the maximum dimension estimated from the autocorrelation function, which was calculated from each diffraction pattern. A random electron density distribution was used as a starting distribution within the support. We used the following equation for a real-space restraint in the HIO iteration [34]:

$$\rho_{k+1}(\vec{r}) = \begin{cases} \rho'_k(\vec{r}) & \vec{r} \in \text{support and } \rho'_k(\vec{r}) \geqslant 0 \\ \rho_k(\vec{r}) - \beta\rho'_k(\vec{r}) & \text{otherwise} \end{cases}, \quad (7)$$

where $\rho_k(\vec{r})$ is the density at the start of the kth cycle, and $\rho'_k(\vec{r})$ is the inverse Fourier transformation for the structure factor with the amplitude from the diffraction pattern and the phase from $\rho_k(\vec{r})$. $\rho_{k+1}(\vec{r})$ is the density for the next cycle, which is prepared using the restraint of Eq. (7). The weight, β, was kept constant at 0.9 throughout the calculation.

The SW algorithm defines the boundary of the support area by excluding areas with densities of less than 5% of the highest density after the convolution of the following Gaussian function to the retrieved image [35]:

$$G(x,y) = \frac{1}{\sqrt{2\pi\alpha^2}} \exp\left[-\frac{x^2+y^2}{2\alpha^2}\right]. \quad (8)$$

The standard deviation α of the Gaussian function was set to 1.5 or 3.0 pixels in the initial stage. After each update of the support area, the value of α was reduced to 0.990–0.995 of that in the previous stage. When the α value became less than 0.90, the value was kept constant at 0.90, as was done in our previous simulation study [14].

The convergence of the phase-retrieval calculation was monitored by the parameter γ [6], which represents the ratio of the total densities inside and outside of the support area, as shown by

$$\gamma = \frac{\sum_{r\notin\text{Support}} \rho(\vec{r})}{(\sigma-1)\sum_{r\in\text{Support}} \rho(\vec{r})}. \quad (9)$$

In the phase-retrieval calculations, we searched for projection images with clear marginal densities and γ values of less than 0.02–0.04 by varying the parameters controlling the HIO and SW calculations, such as the number of HIO cycles before SW update of the support area, and the standard deviation of the Gaussian function used in the SW calculations. In addition, a set of 1000 HIO-only iterations, which was conducted after the completion of the HIO-SW procedure, was powerful enough to make the molecular boundaries of the 50S ribosomal subunits clear. The parameters applied for the phase-retrieval calculations of diffraction patterns are listed in Table I.

The images of 50S ribosomal subunits in the phase-retrieved projection maps were compared with those in the original model, using the correlation coefficient defined by the following equation:

$$r = \frac{\int_{\in 50S}\left\{\rho_{2D}^{\text{original}}(x,y) - \langle\rho_{2D}^{\text{original}}\rangle_{\in 50S}\right\}\left\{\rho_{2D}^{\text{HIO-SW}} - \langle\rho_{2D}^{\text{HIO-SW}}\rangle_{\in 50S}\right\}dxdy}{\sqrt{\int_{\in 50S}\left\{\rho_{2D}^{\text{original}}(x,y) - \langle\rho_{2D}^{\text{original}}\rangle_{\in 50S}\right\}^2 dxdy}\sqrt{\int_{\in 50S}\left\{\rho_{2D}^{\text{HIO-SW}} - \langle\rho_{2D}^{\text{HIO-SW}}\rangle_{\in 50S}\right\}^2 dxdy}},$$
$$\langle\rho_{2D}\rangle_{\in 50S} = \int_{\in 50S}\rho_{2D}(x,y)dxdy \Big/ \int_{\in 50S} dxdy, \quad (10)$$

where $\rho_{2D}^{\text{HIO-SW}}$ and $\rho_{2D}^{\text{original}}$ are the projection density maps of the phase-retrieved and the original models, respectively. The notation of "50S" in the equation represents the pixels that include the atoms of 50S ribosomal subunits. Those pixels were defined from the atomic coordinates of 50S ribosomal subunits in the original models. The correlation function is defined for the fluctuation of the projected density from the average $\langle\rho_{2D}\rangle_{\in 50S}$, which is calculated over the 50S region.

G. 3D reconstruction

3D reconstruction in real space [14,15] was conducted using several protocols in the EMAN suite [36]. After subtracting the average density of the water region from the phase-retrieved projection images, as described in our previous study [14], we selected molecular images of 50S ribosomal subunit from the phase-retrieved projection maps using the *boxer* protocol. In the next step, a Gaussian low-pass filter was used to enhance the molecular

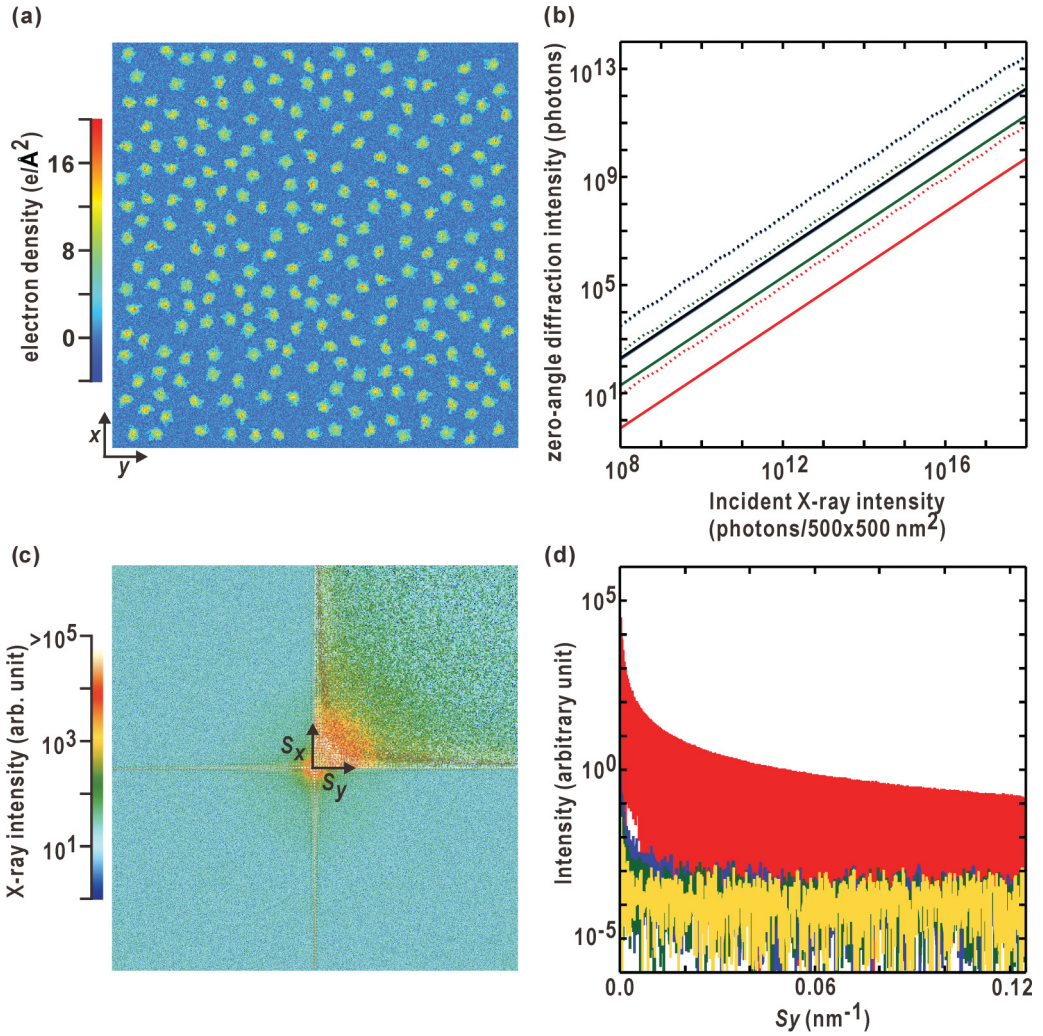

FIG. 4. (Color online) (a) A projection image of a vitreous ice plate including 229 50S ribosomal subunit. (b) Variation of the zero-angle diffraction intensity from the ice plate depending on the intensity of incident x-ray beam with a cross section of 500×500 nm^2. The solid and dotted lines represent intensities calculated for x-ray wavelengths of 0.06 and 0.24 nm, respectively. The intensity values from the entire volume (black, uppermost), particles (red, lowermost), vitreous ice (blue, upper), and their cross terms (green, lower) are displayed. Note that the contribution from the ice plate dominates the observed diffraction intensity. In the calculation, we used the parameters in Eq. (12) as $d = 50$ nm, $a = 500$ nm, $\bar{\rho}_P = 0.62$ $e/$Å^3, $\bar{\rho}_w = 0.33$ $e/$Å^3, $M_P = 1.5$ MDa, $V_M = 0.62 \times 10^{24}$ Å^3/g, $N_P = 229$ molecules, $N_A = 6.0 \times 10^{23}$/mol, and $\sigma = 2$. (c) Diffraction pattern from the ice plate in panel (a) without Poisson noise at a resolution of 0.8 nm at the edge. The upper right quarter is a magnified view of the pattern up to a resolution of 4 nm at the edge. (d) Line profiles of diffraction intensity along S_y at $S_x = 0$ [red (medium gray)], 0.127 [blue (dark gray)], 0.254 [green (medium-dark gray)], and 0.518 nm^{-1} [yellow (light gray)].

boundaries of 50S ribosomal subunits using the *proc2d* protocol (Table I).

We made an initial 3D density model by applying the *startAny* protocol of the EMAN suite to a set of selected projection images, which were obtained by the classification and averaging of projection images using the *refine2d* protocol at a resolution of 3.2 nm. Through the stepwise extension of the resolution limit from 3.2 to 1.6 nm, the density model was improved by applying the *refine* protocol to filtered images after background subtraction. Finally, the 3D-reconstructed model was refined using the projection images without filtering at a full-period resolution of 0.8 nm (Table I).

The effective resolution of the final refined model was estimated from the Fourier shell correlation (FSC) value of 0.143 [37]. The FSC for a given resolution shell S' was defined as follows:

$$\mathcal{F}SC(S') = \frac{\mathrm{Re}\sum_{S\in S'} F_1(S)F_2^*(S)}{\sqrt{\sum_{S\in S'}|F_1(S)|^2 \sum_{S\in S'}|F_2(S)|^2}}, \qquad (11)$$

where $F_1(S)$ [or $F_2(S)$] is the structure factor of the reconstructed density from the half set of the projection images [38].

H. Computation

For the MD simulations, calculations of diffraction patterns, and phase retrieval, we used a cluster machine composed of 4320 cores (AMD Opteron Processor, 2.1 GHz). The computational times for the MD simulation, diffraction pattern, and phase retrieval described in the previous sections

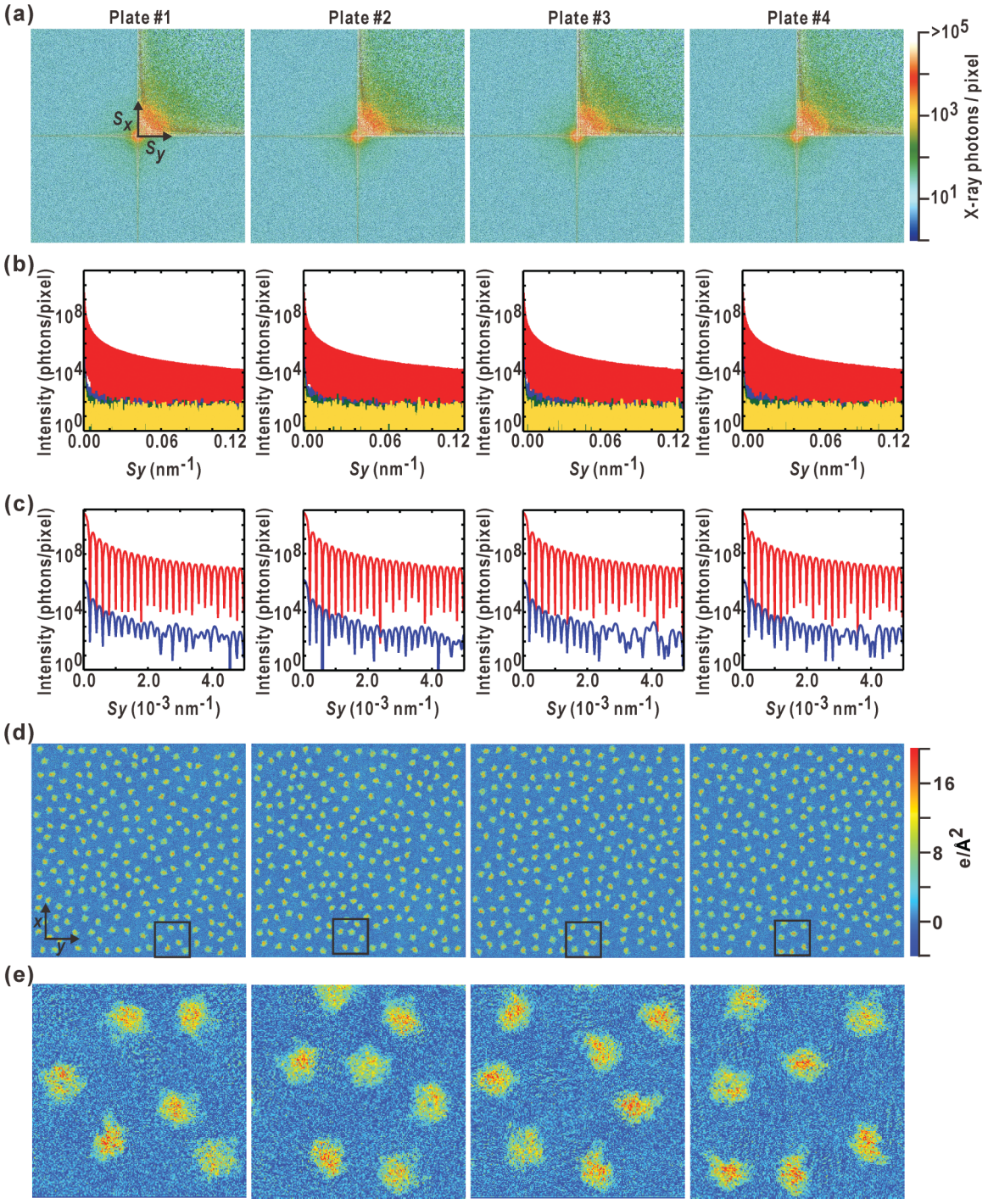

FIG. 5. (Color online) (a) Simulated diffraction patterns of four ice plates up to a resolution of 0.8 nm at the edge of the detector for an incident x-ray intensity of 5×10^{16} photons/500×500 nm^2/pulse. Magnified views of up to 4-nm resolution at the edge are shown in the upper right quarter of the patterns. (b) Line profiles of diffraction intensity along S_y at $S_x = 0$ [red (medium gray)], 0.127 [blue (dark gray)], 0.254 [green (medium-dark gray)], and 0.518 nm^{-1} [yellow (light gray)]. (c) Magnified profiles in panel (b) along $S_x = 0.0$ nm^{-1} (red, upper) and $S_x = 0.127$ nm^{-1} (blue, lower). (d) Projection electron density maps phase-retrieved from the diffraction pattern in panel (a). The average densities of the vitreous ice regions are subtracted. (e) Magnified views of the boxed area in panel (d).

were 25 h/ns, 144 h/plate, and 0.5 h/run, respectively, when using 512 cores. The phase-retrieval computations were conducted using our custom-made and parallelized program [14] that implemented the hybrid-input-output (HIO) [34] and shrink-wrap (SW) algorithms [35]. The 3D reconstruction and other miscellaneous computations were performed using a cluster machine composed of 16 cores (Xeon 5160, 3.0 GHz).

III. RESULTS

Each vitreous ice plate model comprised approximately 429 590 000 water molecules and 20 860 000 atoms belonging to 50S ribosomal subunits [Fig. 4(a)]. The concentration of 50S ribosomal subunits, approximately 46 mg/ml, was in the possible range for biochemically prepared samples.

We first estimated the incident x-ray intensity necessary to record the diffraction pattern using currently available area detectors. Based on the estimated intensity, we conducted calculations of diffraction patterns, phase retrieval, and 3D reconstruction of the electron density model, in that order. In addition, we examined the influences of Poisson noise on the quality of the reconstructed model as well as those of the electron density contrast between 50S ribosomal subunit and vitreous ice in the projection images.

A. Incident x-ray intensity

We calculated the zero-angle diffraction intensity from a thin vitreous ice plate of thickness d irradiated by a square-shaped x-ray beam of dimensions $a \times a$ with uniform intensity I_0.

$$I(\vec{S}=0) = I_0 r_e^2 \left(\frac{\lambda}{\sigma a}\right)^2 \left[\left(N_p \bar{\rho}_p \frac{V_M M_p}{N_A}\right)^2 + \left\{\bar{\rho}_w \left(a^2 d - N_p \frac{V_M M_p}{N_A}\right)\right\}^2 + 2 N_p \bar{\rho}_p \frac{V_M M_p}{N_A} \bar{\rho}_w \left(a^2 d - N_p \frac{V_M M_p}{N_A}\right)\right], \quad (12)$$

where $\bar{\rho}_p$ and $\bar{\rho}_w$ are the average electron densities of the 50S ribosomal subunit and water, respectively. The exclusion volume of the particles was calculated based on the partial specific volume V_M.

Incident x ray with 10^{10} photons/500 × 500 nm^2/pulse is sufficient to record the zero-angle intensity of the vitreous ice plates [Fig. 4(b)], and diffraction intensity in the region from 10- to 0.8-nm resolution was approximately 10^{-8}-fold that of the zero-angle intensity [Figs. 4(c) and 4(d)]. Taking Poisson noise x-ray detection into account, incident x-ray intensity of greater than approximately 10^{15} photons/500 × 500 nm^2/pulse is necessary to collect diffraction patterns with a high signal-to-noise ratio under an oversampling ratio of 2 × 2. Thus, we performed the simulation under incident x ray of 5×10^{16} photons/500 × 500 nm^2/pulse.

B. 3D reconstruction of 50S ribosomal subunit

The diffraction pattern of each vitreous ice plate displayed a characteristic cross shape [Figs. 5(a)–5(c)], which can be approximated by the Fraunhofer diffraction of a square-shaped object [39] with a width of 500 nm and uniform density. The width of the sample was experimentally estimated using a series of diffraction minima along the equator and meridian [Fig. 5(c)]. In addition, the theoretical diffraction pattern contains an approximation of the region near the zero angle, which is lost experimentally due to a beamstop blocking the direct beam. Contributions from the structure factors of 50S ribosomal subunit were appreciable in the off-meridional and off-equator regions, when comparing with the pattern from vitreous ice alone [Fig. 2(c)]. The diffraction intensity varied from 10^{11} to 10^{1} photons/pixel, requiring an array of area detectors covering a range of different scattering vectors.

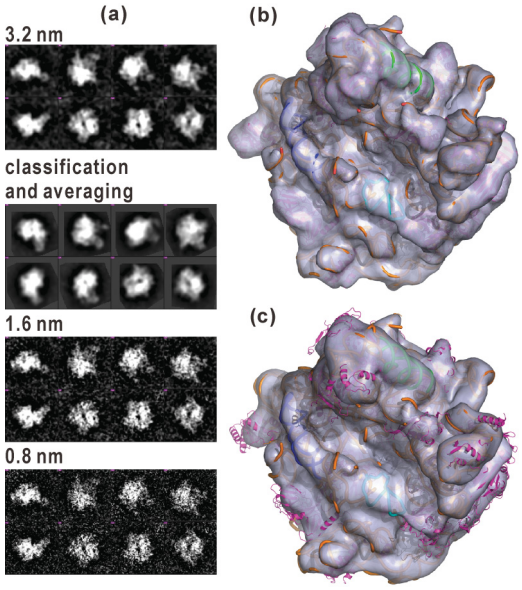

FIG. 6. (Color online) (a) Typical projection images used in the 3D reconstruction of the 50S ribosomal subunit. In all images used for 3D reconstruction, the average electron density of the vitreous ice region is subtracted from the phase-retrieved images. Shown from upper to lower are the low-pass filtered images at 3.2-nm resolution, classified and averaged images for constructing the initial model at 3.2-nm resolution, low-pass filtered images at 1.6-nm resolution, and the raw images at 0.8-nm resolution. (b) The 3D electron density model calculated directly from the crystal structure of the 50S ribosomal subunit [27]. (c) The 3D-reconstructed density model from 1832 projection images at a resolution of 1.6 nm. The density models in panels (b) and (c) are contoured at one standard deviation level from the average. These panels were prepared using PYMOL [52].

Each projection image retrieved at a resolution of 0.8 nm was composed of a 500 × 500 nm^2 ice region and 229 images of the 50S ribosomal subunits [Fig. 5(d)]. No mirror images of the ice plate models were retrieved. The correlation coefficient between the electron density maps of the phase-retrieved and the original models was about 0.86–0.90 for 50S ribosome regions (Table I), probably because of Poisson noise and the electron density contrast against the ice region. Several structural characteristics of the 50S ribosomal subunits were visible, including the tunnel polypeptide exit, the protuberance of 5S ribosomal RNA, and the crown shape [Fig. 5(e)].

In the initial stage in the 3D reconstruction, it was easy to construct the starting model at a resolution of 3.2 nm rather than at 0.8 nm. The noise-smeared projection images lost structural details of the 50S subunit and were therefore unsuitable to roughly estimate the 3D density [Fig. 6(a)]. During the 3D-reconstruction procedure, we compared the density model with that directly calculated from the crystal structure [Figs 6(b) and 6(c)]. The calculated density enveloped all ribosomal RNA proteins and displayed grooves in

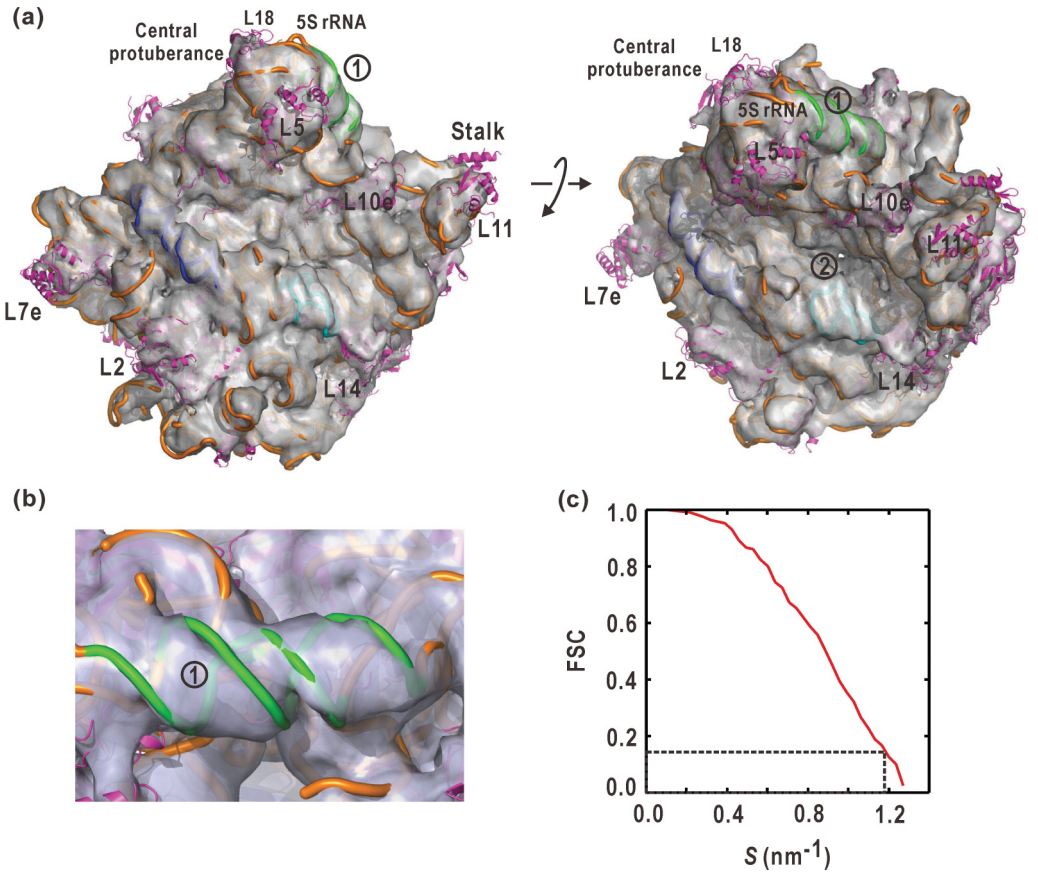

FIG. 7. (Color online) (a) Reconstructed electron density model of the 50S ribosomal subunit (gray-colored and surface-rendered) superimposed on the crystal structure solved at a resolution of 0.22 nm [27]. The density is contoured at the 1.5 standard deviation level from the average. In the crystal structure model, ribosomal RNAs are depicted as orange, cyan, blue, and green tubes, and ribosomal proteins are displayed as magenta-colored ribbon models. Several structurally characteristic regions, ribosomal RNAs, and proteins are labeled. The left panel shows a typical "crown" view of the 50S ribosomal subunit with a protuberance of 5S RNA (symbol 1), and the right panel shows the characteristic peptide tunnel (symbol 2). (b) An electron density map of the 5S ribosomal RNA forming the protuberance compared with the crystal structure model [green (light gray) tube]. (c) A graph plotting FSC for the reconstructed density model of panel (a) against the resolution. The dashed line indicates a FSC value of 0.143.

double-stranded RNA, while the reconstructed density model lacked those characteristics.

Figure 7(a) shows two views of the final density model of the 50S ribosomal subunit obtained by applying the 3D-reconstruction method to the 1832 projection images from eight ice plates. In the density model, we identified structural characteristics of the 50S ribosomal subunit [Figs. 7(a) and 7(b)] previously found in x-ray crystallography and EM analyses [40,41], such as a crown shape with a large crevice of the active-site cleft, the narrow peptide tunnel running from this crevice to the back face of the subunit, and the double-stranded helices of several ribosomal RNAs. As a typical example, the reconstructed electron density of the 5S ribosomal RNA, which forms the central protuberance of the 50S ribosomal subunit, is presented in Fig. 7(b). The effective resolution of the model, as estimated by the FSC value of 0.143 [37], is approximately 0.9 nm [Fig. 7(c)].

The electron density of ribosomal proteins located at the surface of the 50S ribosomal subunit was partly invisible [Figs. 6(c), 7(a), and 7(b)]. We expect radiation damage [42], Poisson noise, and differences in the electron density contrast between particles to limit our ability to accurately estimate the electron density of proteins located on the 50S ribosomal subunit surface. The errors in electron density in the phase-retrieved projection images directly impact the lack of the structural details necessary to unambiguously determine the orientation of particles to the incident x-ray beam. The ambiguity in the orientation of each particle in turn results in 3D models with tapered shapes. These points were examined as described in the following sections.

C. Influence of Poisson noise on 3D reconstruction

We qualitatively examined the influences of Poisson noise on 3D-reconstructed electron density models by varying x-ray wavelength and incident intensity applied to the eight ice plates (Fig. 8 and Table II). Even in a reference simulation without Poisson noise (simulation 1 in Fig. 8 and Table II), the 3D-reconstructed density model lost the features of ribosomal proteins, likely due to the contrast between the 50S ribosomal subunits and the vitreous ice region, as discussed in the next section.

Through simulations under different incident intensity and wavelength of x rays, we found that the quality of the

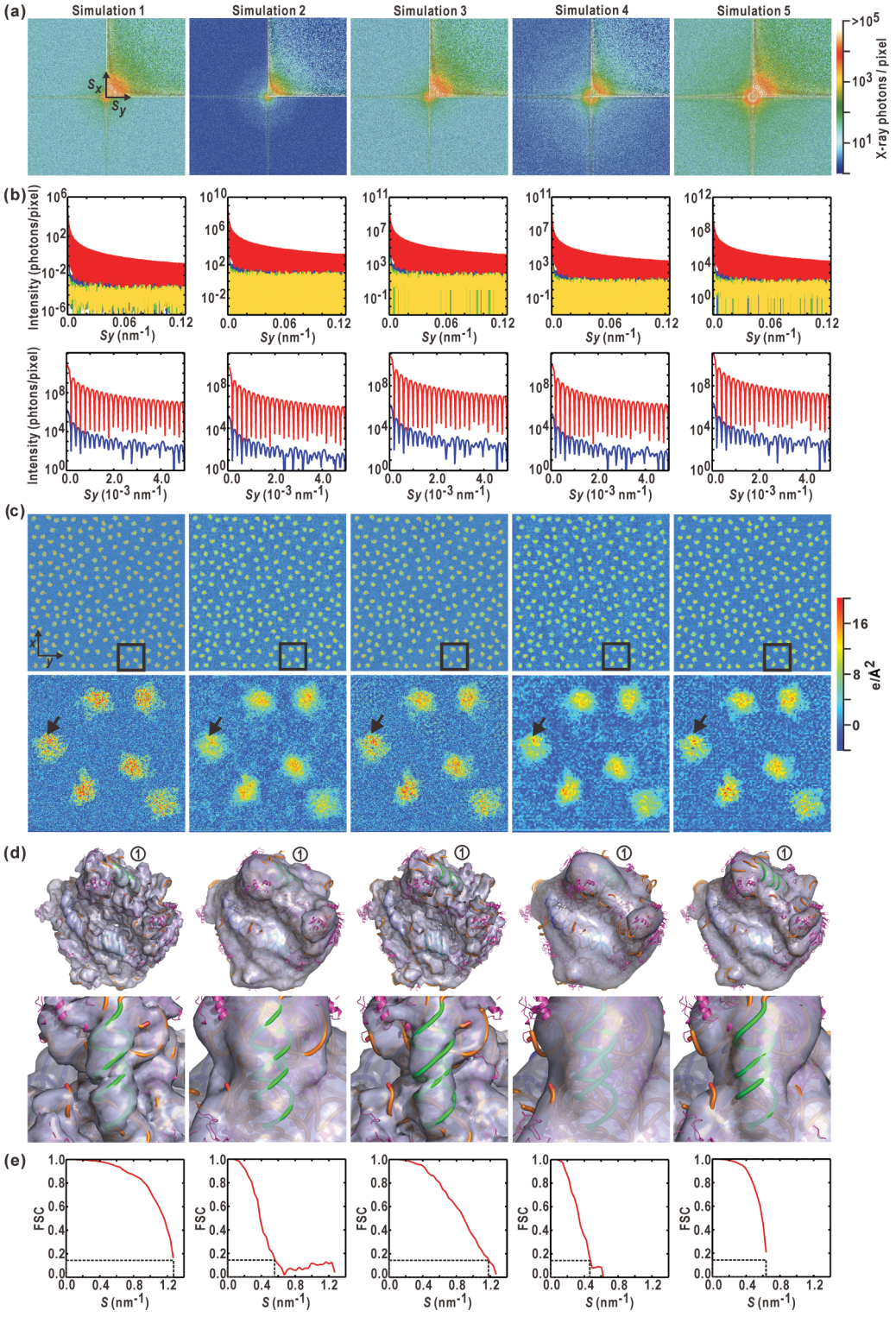

FIG. 8. (Color online) Effects of Poisson noise and x-ray wavelength on 3D-reconstructed density maps. Shown for each simulation: (a) the diffraction pattern, (b) line profiles as drawn in panels (b) and (c) in Fig. 5, (c) whole (upper) and magnified (lower) views of phase-retrieved projection images, (d) the 3D-reconstructed electron density model of the 50S ribosomal subunit (upper) and 5S RNA forming the protuberance (lower), and (e) the FSC curve used to estimate the effective resolution. The coloring (gray scale) scheme in the panels is the same as that used in Figs. 5 and 7. The parameters used in the simulations are summarized in Table II.

phase-retrieved projection map depended heavily on the diffraction intensity beyond 0.05 nm^{-1}. For instance, projection images of the 50S ribosomal subunit in simulation 2 lacked the peptide tunnel, whereas the corresponding image in simulation 3, in that a tenfold stronger incident intensity (5×10^{16} photons/500×500 nm^2/pulse) was assumed,

TABLE II. Parameters used in the simulations with and without Poisson noise for ice plates with a volume of $0.5 \times 0.5 \times 0.05\ \mu m^3$.

Simulation	1	2	3	4	5
Diffraction patterns	Noiseless	Poisson noise	Poisson noise	Poisson noise	Poisson noise
Number of ice	8	8	8	8	8
Size of diffraction pattern (pixels)	2560×2560	2560×2560	2560×2560	1280×1280	1280×1280
OS ratio (S_x and S_y directions)	4 (2,2)	4 (2,2)	4 (2,2)	4 (2,2)	4 (2,2)
S/pixel (nm^{-1})	9.95×10^{-4}	9.95×10^{-4}	9.95×10^{-4}	9.95×10^{-4}	9.95×10^{-4}
Maximum S (nm^{-1})	1.27	1.27	1.27	6.37×10^{-1}	6.37×10^{-1}
X-ray wavelength (nm)	0.06	0.06	0.06	0.24	0.24
Incident x-ray intensity (photons/$500 \times 500\ nm^2$/pulse)	5.0×10^{11}	5.0×10^{15}	5.0×10^{16}	5.0×10^{14}	5.0×10^{15}
I ($S = 0$)	6.74×10^5	6.74×10^9	6.74×10^{10}	1.08×10^{10}	1.08×10^{11}
Phase retrieval					
Size of the support (pixels)	1280×1280	1280×1280	1280×1280	640×640	640×640
Width of the pixels (nm)	3.93	3.93	3.93	7.85	7.85
Number of support update cycle	2500	2500	2500	2500	2500
HIO cycles per support update	4, 5, 10, 20	4, 5, 10, 20	4, 5, 10, 20	4, 5, 10, 20	4, 5, 10, 20
Initial SW parameter α	3.0	1.5, 3.0	1.5, 3.0	1.5, 3.0	1.5, 3.0
Reduction rate of α after every support update	0.995	0.990, 0.995	0.990, 0.995	0.990, 0.995	0.990, 0.995
Final γ (%)	0.209–0.247	0.648–0.774	0.380–0.403	0.385–0.566	0.264–0.427
Correlation between the original and retrieved images	0.92–0.94	0.79–0.80	0.86–0.90	0.93–0.94	0.97–0.98
3D reconstruction					
Parameter of Gaussian low-pass filter	9–36	9–18	9–36	9–18	9–18
Resolution of projection images in the final refinement (nm)	0.393	1.57	0.393	1.57	0.785
Estimated resolution from the FSC value of 0.143 (nm)	0.782	1.77	0.842	2.12	1.55

retained the detail [Fig. 8(d)]. The quality of the projection images [Fig. 8(c)] correlated with the ambiguity in determining the orientation of the 50S ribosomal subunit to incident x ray. Thus, the 3D-reconstructed density model in simulation 2 was tapered significantly in comparison with that in simulation 3. Because of the nature of Poisson noise, only the tenfold difference in the incident intensity between simulations 2 and 3 drastically changes the quality of the 3D-reconstructed density model. At least, a diffraction intensity of 10^2/pixel in the highest resolution is necessary to prevent the loss of structural details in 3D reconstruction [Fig. 8(b)]. In simulation 3, the 3D-reconstructed models were qualitatively similar to that of simulation 1 (without Poisson noise), as several characteristics of the 50S ribosomal subunit, including the peptide tunnel and grooves of the double-stranded ribosomal RNA (Fig. 7).

According to Eq. (1), longer wavelength is a choice to increase the diffraction intensity as demonstrated in simulations 4 and 5 for a 0.24-nm x ray. As observed in the simulations for a 0.06-nm x ray, the tenfold stronger incident intensity resulted in the drastic changes in the quality of the 3D-reconstructed density model (Fig. 8). In simulation 4, the diffraction intensity displayed a slightly higher intensity than that of simulation 2; however, the peptide tunnel in the phase-retrieved image became invisible. The reconstructed electron density model is similar to the shape proposed in early structural studies of the 50S ribosomal subunit using negatively stained electron microscopic images [43]. Simulation 5 was performed using an x-ray intensity of 5×10^{15} photons/$500 \times 500\ nm^2$/pulse. The structural characteristics of the 3D-reconstructed density model in simulation 5 became clearer than those in simulation 4. However, even with the long wavelength, the phase-retrieved image and density model are similar to those obtained in simulation 2. This is because of the limited area of detector assumed in this simulation.

The estimated resolution from the FSC values supports the fact that the structural characteristics of the 3D-reconstructed density models are in accordance with those of molecular shapes and structures of the 50S ribosomal subunit, which were determined in the past [40,41,43]. It should be noted here that the γ value can be used to judge the reliability of phase-retrieved images. In simulations 2 and 4, in which the phase-retrieved images lost structural details, the γ values of retrieved images tended to be higher than those of simulations 3 and 5. Thus, the γ value may be an important indicator to measure the effects of Poisson noise.

D. Influence of electron density contrast

The 3D-reconstructed density models, even those from the noiseless diffraction patterns, lack structural details of some parts in the ribosomal proteins (simulation 1 in Fig. 8). This probably came from the electron density contrast between

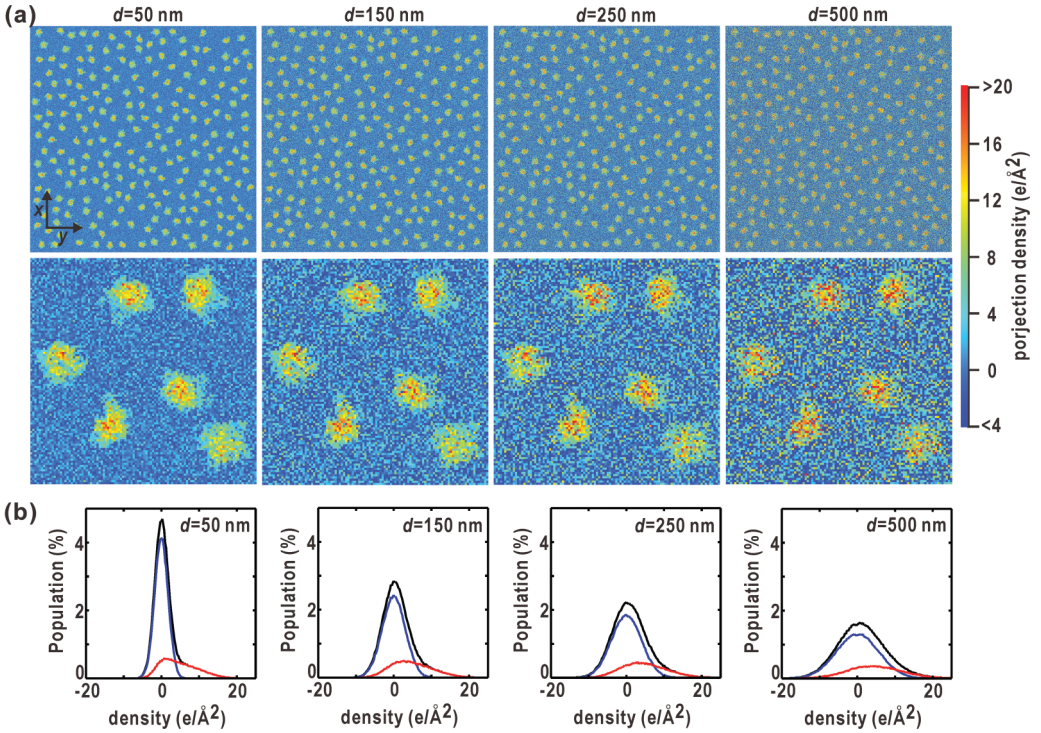

FIG. 9. (Color online) (a) Comparison of the contrast between the 50S ribosomal subunit and vitreous ice region in ice plates with a thickness of 50, 150, 250, and 500 nm. The upper panels show the projection electron density maps of 500×500 nm^2, and the lower panels show a magnified view of the upper. (b) Histograms of electron densities over the entire (black line), vitreous ice [blue (dark gray)], and 50S ribosomal subunit regions [red (medium gray)].

the 50S ribosomal subunit and the vitreous ice region in the projection maps as we discussed in the previous study [14]. We quantitatively examined this point through comparing the projection maps of the ice plate models with thicknesses in the range of 50–500 nm [Fig. 9(a)].

Up to a thickness of 150 nm, the projection images of the 50S ribosomal subunit were similar to those observed for an ice plate of 50-nm thickness. In plates with a thickness of greater than 250 nm, the border between the 50S ribosomal subunit and the ice region became unclear. In addition, the electron density distribution inside the 50S ribosomal subunit displayed low correlation with that observed in the ice plate of 50-nm thickness, because the distribution was modified by the accumulated electron density fluctuation in the vitreous ice volumes sandwiching a 50S ribosomal subunit along the direction of the incident x ray.

Histograms of the electron density might be helpful to quantitatively understand the observed variation [Fig. 9(b)]. For the 50-nm-thick ice plate, the histogram of the water region is within $\pm 5\ e/\text{Å}^2$ from the average, while that of the 50S ribosomal subunit is in the range of -5 to $17\ e/\text{Å}^2$. With increasing the thickness of the ice plate, the histogram of the ice region exhibited significant broadening to $\pm 10\ e/\text{Å}^2$, whereas that of the 50S ribosomal subunit extended slightly towards the negative. This difference in the broadening of the histograms likely reduced the contrast between the 50S ribosomal subunit and the ice region. Together, these suggest that an ice plate with a thickness of less than 170 nm will give sufficient contrast to reconstruct structural detail in the projection images.

IV. DISCUSSION

Currently, XFEL sources provide coherent and intense x-ray pulses in the range of 10^{12}–10^{13} photons/μm^2/pulse after focusing. However, due to the small scattering cross section of electrons for x rays, the available incident x-ray intensity of XFEL sources is lower than that necessary to perform single-shot diffraction experiments for noncrystalline biomolecules with the molecular masses of megadalton and submicrometer dimensions. Here, we propose a protocol for visualizing the structure of those biomolecules by the combinational application of the coherent x-ray diffraction imaging and 3D-reconstruction methods to thin vitreous ice plates containing several hundred particles/μm^2. The vitreous ice sample will have a far larger scattering cross section than a single particle. The feasibility of the protocol was examined through simulations performed at a resolution of 0.8 nm for the 3D reconstruction of the 50S ribosomal subunit embedded in vitreous ice plates with a volume of $500 \times 500 \times 50$ nm^3.

A. Benefit of the protocol

The results of our present simulations have revealed that for XFEL-CXDI experiments for biomolecules in vitreous ice plate, it is better to use ice plates as thin as possible with short and strong x-ray pulses. For instance, as the low contrast in the thick ice plate causes significant modification to the projected densities of the 50S ribosomal subunit, the ice plates should ideally have a thickness of less than six times the maximum dimension of the 50S ribosomal subunit.

The use of a large number of particle images is one of the approaches for reducing the ambiguity in determining the orientation of the 50S ribosomal subunit in projection images in 3D reconstruction. Our proposed protocol enables the collection of a large number of particle images within a short period of time from a small volume of the sample suspension, and is free from the positional instability of an x-ray beam at the sample position (Fig. 1). For instance, when we obtain diffraction patterns from a 30×30 array of irradiation areas on a vitreous ice plate containing 50S ribosomal subunits at the same concentration as seen in Fig. 2(a), the translational movement of the ice plate against XFEL pulses of 10 Hz would ideally give 207 000 images of the 50S ribosomal subunit in various orientations within 90 s.

In the present simulation, we assumed the incident x-ray intensity of 5×10^{14}–5×10^{16} photons/500×500 nm^2/pulse, which is far larger than the currently available XFEL intensity of 10^{12}–10^{13} photons/μm^2/pulse. Therefore, to realize noncrystalline biomolecule diffraction imaging of a 50S ribosomal subunit as proposed here, we need the more intense beam, which will be realized by the self-seeding of the XFEL source [44,45] and the new technology of x-ray focusing mirror [13]. For structural analyses with the currently available XFEL sources, particles with higher electron densities than the 50S ribosomal subunit should be suitable.

In this simulation, we assumed rigid structure of the 50S ribosomal subunit; however, biological macromolecular assemblies possess their own characteristic dynamics. Through a huge number of images, the reconstruction methods of macromolecular dynamics have been theoretically proposed in recent years [7,46]. For that purpose, our protocol can provide a huge number of images of particles in the dynamical motions for a multiple data analysis method proposed recently [46].

B. Instrumentation suitable to conduct the protocol

Toward performing XFEL-CXDI analyses according to the protocol proposed here (Fig. 1), it is necessary to consider what kinds of sample preparation method, diffractometer, and detector are suitable. Regarding sample preparation, sample suspensions with concentrations as high as possible will facilitate collection of a higher number of projection images, and vitreous ice plates are as thin as possible to ensure sufficient contrast in electron density. Thin vitreous ice plates can be prepared by flash cooling thin water plates, which may be formed in 200–300-μm pinholes fabricated in 3-mm-diameter stainless disks under a humidity-controlled atmosphere [47]. When performing diffraction experiments, flash-cooled samples must be kept in a vacuum at temperatures below 77 K to avoid the melting and frosting of the flash-cooled sample. Thus, the diffraction apparatus dedicated to the cryogenic experiment should be composed of a sample stage and a sample loading device to carry flash-cooled samples to the stage. The stage should be kept at liquid nitrogen temperature connected to an in-vacuum-type goniometer. A simple modification of a conventional EM cryoholder is possible, but a dedicated apparatus may be more suitable and convenient for XFEL-CXDI [48,49].

To collect diffraction patterns at a resolution of 0.8 nm and with an oversampling ratio of 2×2 for a sample with a cross section of 500×500 nm^2, a detector with 2560 pixels is required. Because it may be difficult to manufacture a single detector that is able to cover the required area, an array of detectors is necessary. The beamstop and other detector parts needed to prevent parasitic scattering, as well as the gaps between detectors, results in the loss of signal in specific regions of the acquired diffraction patterns, particularly in small-angle regions that are indispensable for phase-retrieval calculation. When using a vitreous ice plate as the container of the immobilized sample particles, the resulting diffraction patterns are influenced by the shape and intensity distribution of the incident x-ray beam. Thus, diffraction intensities absent in recorded patterns can be approximated by theoretical or numerical calculations. In addition, the use of algorithms, such as an algorithm for dark-field imaging [50] and/or pseudopolar Fourier transform [51], may be useful in overcoming the loss of data in diffraction patterns.

ACKNOWLEDGMENTS

The authors thank Dr. Greg Newton and Dr. Jose A. Rodriguez of UCLA for valuable comments for polishing our manuscript. This work was supported by X-Ray Free Electron Laser Priority Strategy Program (MEXT) and by Kakenhi from MEXT, Japan (Grant No. 22244054) and JSPS, Japan (Grants No. 22018027 and No. 24654140 to M.N., and Grant No. 24113723 to T.O.).

[1] J. Miao, D. Sayre, and H. N. Chapman, J. Opt. Soc. Am. A **15**, 1662 (1998).
[2] J. Miao, P. Charalambous, J. Kirz, and D. Sayre, Nature (London) **400**, 342 (1999).
[3] J. Miao, T. Ishikawa, Q. Shen, and T. Earnest, Annu. Rev. Phys. Chem. **59**, 387 (2008).
[4] H. N. Chapman and K. A. Nugent, Nat. Photonics **4**, 833 (2010).
[5] I. Robinson and R. Harder, Nat. Mater. **8**, 291 (2012).
[6] J. Miao, K. O. Hodgson, and D. Sayre, Proc. Natl. Acad. Sci. USA **98**, 6641 (2001).
[7] R. Fung, V. Shneerson, D. K. Saldin, and A. Oumazd, Nat. Phys. **5**, 64 (2009).
[8] K. S. Raines, S. Salha, R. L. Sandberg, H. Jiang, J. A. Rodriguez, B. P. Fahimian, H. C. Kapteyn, J. Du, and J. Miao, Nature (London) **463**, 214 (2010).
[9] P. Emma *et al.*, Nat. Photonics **4**, 641 (2010).
[10] T. Ishikawa *et al.*, Nat. Photonics **6**, 540 (2012).
[11] M. M. Seibert *et al.*, Nature **470**, 78 (2011).
[12] U. Weierstall, R. B. Doak, J. H. C. Spence, D. Starodub, D. Shapiro, P. Kennedy, J. Warner, G. G. Hembree, P. Fromme, and H. N. Chapman, Exp. Fluids **44**, 675 (2008).
[13] H. Mimura, S. Morita, T. Kimura, D. Yamakawa, W. Lin, Y. Uehara, S. Matsuyama, H. Yumoto, H. Ohashi, K. Tamasaku, Y. Nishino, M. Yabashi, T. Ishikawa, H. Ohmori, and K. Yamauchi, Rev. Sci. Instrum. **79**, 083104 (2008).

[14] W. Kodama and M. Nakasako, Phys. Rev. E **84**, 021902 (2011).
[15] J. Frank, *Three-Dimensional Electron Microscopy of Macromolecular Assemblies* (Oxford University Press, Oxford, 2006).
[16] G. Huldt, A. Azke, and J. Hajdu, J. Struct. Biol. **144**, 219 (2003).
[17] V. L. Shneerson, A. Ourmazd, and D. K. Saldin, Acta Crystallogr., Sect. A **64**, 303 (2008).
[18] Z. Kam, Macromolecules **10**, 927 (1977).
[19] D. K. Saldin, H. C. Poon, M. J. Bogan, S. Marchesini, D. A. Shapiro, R. A. Kirian, U. Weierstall, and J. C. H. Spence, Phys. Rev. Lett. **106**, 115501 (2011).
[20] T. A. Steitz, Nat. Rev. Mol. Cell Biol. **9**, 242 (2008).
[21] N. Ban, P. Nissen, J. Hansen, P. B. Moore, and T. A. Steitz, Science **289**, 905 (2000).
[22] W. L. Jorgensen, J. Chandrasekhar, J. D. Madura, R. W. Impey, and M. L. Klein, J. Chem. Phys. **79**, 926 (1983).
[23] M. Ikeguchi, J. Comput. Chem. **25**, 529 (2004).
[24] T. Darden, D. York, and L. Pedersen, J. Phys. Chem. **98**, 10089 (1993).
[25] T. F. Miller III, M. Eleftheriou, P. Pattnaik, A. Ndriango, D. Newns, and G. J. Martyna, J. Chem. Phys. **116**, 8649 (2002).
[26] G. J. Martyna, D. J. Tobias, and M. L. Klein, J. Chem. Phys. **101**, 4177 (1994).
[27] T. M. Schmeing, K. S. Huang, D. E. Kitchen, S. A. Strobel, and T. A. Steitz, Mol. Cell **20**, 437 (2005).
[28] A. Ponti, Magn. Reson. **138**, 288 (1999).
[29] D. Matsuoka and M. Nakasako, J. Phys. Chem. B **113**, 11274 (2009).
[30] J. Drenth, *Principles of Protein X-ray Crystallography* (Springer-Verlag, New York, 1994).
[31] D. Sayre, Acta Crystallogr. **5**, 843 (1952).
[32] *International Tables for X-Ray Crystallography*, Vol. IV (Kynoch Press, Birmingham, UK, 1974), p. 71 (present distributor D. Riedel, Dordrecht).
[33] H. P. William, A. T. Saul, T. V. William, and P. F. Brian, *Numerical Recipes in C: The Art of Scientific Computing*, 2nd ed. (Cambridge University Press, Cambridge, 1992).
[34] J. R. Finup, Appl. Opt. **21**, 2758 (1982).
[35] S. Marchesini, H. He, H. N. Chapman, S. P. Hau-Riege, A. Noy, M. R. Howells, U. Weierstall, and J. C. H. Spence, Phys. Rev. B **68**, 140101 (2003).
[36] S. J. Ludtke, P. R. Baldwin, and W. Chiu, J. Struct. Biol. **128**, 82 (1999).
[37] P. B. Rosenthal and R. Henderson, J. Mol. Biol. **333**, 721 (2003).
[38] M. van Heel and M. Schatz, J. Struct. Biol. **151**, 250 (2005).
[39] M. Born and E. Wolf, *Principles of Optics*, 7th ed. (expanded) (Cambridge University Press, Cambridge, 1999).
[40] N. Ban, B. Freeborn, P. Nissen, P. Penczek, R. A. Grassucci, R. Sweet, J. Frank, P. B. Moore, and T. A. Steitz, Cell **93**, 1105 (1998).
[41] N. Ban, P. Nissen, J. Hansen, M. Capel, P. B. Moore, and T. A. Steitz, Nature **400**, 841 (1999).
[42] H. M. Quiney and K. Nugent, Nat. Phys. **7**, 142 (2011).
[43] M. Radermacher, T. Wagenknecht, A. Verschoor, and J. Frank, EMBO J. **6**, 1107 (1987).
[44] J. Amann *et al.*, Nat. Photonics **6**, 693 (2012).
[45] G. Geloni, V. Kocharyan, and E. Saldin, DESY 10-053 (2010).
[46] P. Schwander, D. Giannakis, C. H. Yoon, and A. Ourmazd, Opt. Express **20**, 12827 (2012).
[47] Y. Takayama and M. Nakasako, Rev. Sci. Instrum. **83**, 054301 (2012).
[48] X. Huang, J. Nelson, J. Kirz, E. Lima, S. Marchesini, H. Miao, A. M. Neiman, D. Shapiro, J. Steinbrener, A. Stewart, J. J. Turner, and C. Jacobsen, Phys. Rev. Lett. **103**, 198101 (2009).
[49] E. Lima, L. Wiegart, P. Pernot, M. Howells, J. Timmins, F. Zontone, and A. Madsen, Phys. Rev. Lett. **103**, 198102 (2009).
[50] A. V. Martin *et al.*, Opt. Express **20**, 13501 (2012).
[51] C. C. Chen, C. H. Lu, D. Chien, J. Miao, and T. K. Lee, Phys. Rev. B **84**, 024112 (2011)
[52] W. L. DeLano, computer code pymol (DeLano Scientific, Palo Alto, CA, 2002), http://www.pymol.org